Computer Modeling in Engineering & Sciences

Tech Science Press

DOI: 10.32604/cmes.2023.027745

ARTICLE

Chaotic Motion Analysis for a Coupled Magnetic-Flow-Mechanical Model of the Rectangular Conductive Thin Plate

Xinzong Wang[1], Xiaofang Kang[1,2,*] and Qingguan Lei[1]

[1]School of Civil Engineering, Anhui Jianzhu University, Hefei, 230601, China

[2]Key Laboratory of Intelligent Underground Detection Technology, Anhui Jianzhu University, Hefei, 230601, China

*Corresponding Author: Xiaofang Kang. Email: xiaofangkang@ahjzu.edu.cn

Received: 13 November 2022 Accepted: 13 February 2023 Published: 28 June 2023

ABSTRACT

The chaotic motion behavior of the rectangular conductive thin plate that is simply supported on four sides by airflow and mechanical external excitation in a magnetic field is studied. According to Kirchhoff's thin plate theory, considering geometric nonlinearity and using the principle of virtual work, the nonlinear motion partial differential equation of the rectangular conductive thin plate is deduced. Using the separate variable method and Galerkin's method, the system motion partial differential equation is converted into the general equation of the Duffing equation; the Hamilton system is introduced, and the Melnikov function is used to analyze the Hamilton system, and obtain the critical surface for the existence of chaos. The bifurcation diagram, phase portrait, time history response and Poincaré map of the vibration system are obtained by numerical simulation, and the correctness is demonstrated. The results show that when the ratio of external excitation amplitude to damping coefficient is higher than the critical surface, the system will enter chaotic state. The chaotic motion of the rectangular conductive thin plate is affected by different magnetic field distributions and airflow.

KEYWORDS

Rectangular conductive thin plate; chaotic; airflow; magnetic field; Melnikov function; Galerkin's method

1 Introduction

With the advancement and development of modern high-tech, devices with magnetic, electrical, and other materials as structures are frequently used. Rectangular thin plates are widely used in road and bridge construction, machinery industry, ship engineering, aerospace, and other fields. When the system is disturbed by the outside world, it will not only produce periodic linear dynamic behavior, but also show chaotic motion behavior to a large extent, resulting in the failure of the system under repeated loads. At present, there are two very popular directions for the study of nonlinear dynamics of structures such as thin plates at home and abroad. One is the study of nonlinear aeroelastic problems, the other is the study of nonlinear electromagnetic elasticity aspects.

The study of geometric nonlinear aeroelasticity differs from general aeroelasticity [1] from the theoretical aspects as follows: One is the structural geometric nonlinear theory, which mainly addresses the static and dynamic analysis of the structure under large deformation [2–4]; The other

is the study of surface aerodynamic theory [5], which mainly addresses the boundary condition dependent deformation state aerodynamic calculation method under large deformation conditions of the structure [6]; The third is the study of the structural/aerodynamic interface coupling method [7,8], which mainly investigates the multidimensional interpolation problem applicable to large deformation in space. The problem of subsonic aeroelasticity of plates focuses on the fluid-structure coupling between the structure and the airflow [9,10]. The variety of parameters, such as mass, damping and stiffness of the structure under the action of subsonic airflow affects the critical instability and nonlinear vibration characteristics of the structure [2,11]. The assumption of small deformation in its research is no longer applicable, the equilibrium state of the structure after force deformation presents obvious geometric differences relative to the undeformed structure, and the geometric nonlinear factors caused by the load-bearing and deformation state of the structure make the structural static and dynamic characteristics change, and change the static and dynamic aeroelastic coupling relationship, thus making the research and application of aeroelasticity face new challenges.

The theory of electromagnetic elasticity is devoted to the study of the coupling of electromagnetic fields with deformation fields. This theory is basically a coupling of the theory of linear elasticity [12] and the theory of linear electrodynamics in a free moving medium. If the studied elastomer is located in an initially strong magnetic field, mechanical and thermal loads would generate an electromagnetic field while causing a deformation field. The two fields will interact and influence each other and a coupling mechanism will occur. The action of the electromagnetic field on the deformation field is caused by the Lorentz force in the equations of motion [13–15]. The deformation field affects the strength of the magnetic field, the magnetoelastic wave [16] and the propagation velocity of the electromagnetic wave, and the item depends on the displacement velocity of the deformed object in the magnetic field [17]. Extensive research on the theory of magnetoelastic nonlinear problems in electromagnetic structures is important for the dynamic analysis of structural elements at high temperatures [18–20], high pressures and under the action of strong electromagnetic fields. For example, Liu et al. [21,22] performed numerical simulations using the pseudo-arclength continuation algorithm to analyze the effects of external temperature variations, magnetic potential, electrical potential, and excitation amplitude on the nonlinear vibration response of composite cylindrical shells. When the electromagnetic structure is in an applied electromagnetic field environment, on one hand, the electromagnetic structure is deformed by the electromagnetic force [23,24], and on the other hand, the deformation of the structure leads to a change in the electromagnetic field and thus to a change in the distribution of the electromagnetic force. For the current-carrying conductor [25], the electromagnetic force is the Lorentz force. For polarizable or magnetizable electromagnetic dielectric materials, the electromagnetic force is generated by the interaction of the polarization or magnetization [26] with the external electromagnetic field. A fundamental feature of this mutual coupling of the electromagnetic and mechanical fields is the nonlinearity. Even if the electromagnetic and mechanical fields are treated as linear separately, the coupled electromagnetic-elastic mechanical marginal equations are still nonlinear. Therefore, the study of their nonlinear kinematic states has also become an inevitable trend [27–29]. However, studies in either nonlinear electromagnetic elasticity or nonlinear aeroelasticity have focused on their respective areas of expertise without considering the coupling effects of these two cases. The theory is more complex when considering the combined effect of airflow and periodic excitation on the vibration characteristics of a system under the action of a magnetic field, and there are still many issues to be investigated.

In this paper, the basic assumptions of Kirchhoff's theory are used, geometric nonlinearities are considered, and the nonlinear equations of motion of a magnetoelastic rectangular thin plate with simple support on four sides are established using the principle of imaginary work. The Hamiltonian

is analyzed with the Melnikov function and the conditions under which the motion exhibits chaotic behavior are obtained. The bifurcation diagram, phase portrait, time history response and Poincaré map of the system were simulated with MATLAB software. The effects of the magnetic field environment as well as the airflow on the chaotic motion of the magnetoelastic rectangular thin plate are also analyzed.

2 Differential Equations of Rectangular Conductive Thin Plate under the Action of External Excitation in Magnetic Field

Consider a four-sided simply supported rectangular conductive thin plate under the action of airflow and periodic mechanical excitation in the magnetic field environment shown in Fig. 1. The length, width and thickness of the plate, respectively a, b and h, satisfy that the thickness is much smaller than the minimum value of the length and width. Taking the middle surface of the plate as the XY plane, establish the coordinate system shown in Fig. 1. x, y and z denote the x-axis, y-axis and z-axis, respectively, U denotes the incoming flow velocity, P_z and B_{1z} denote the mechanical surface force and magnetic field distribution, respectively.

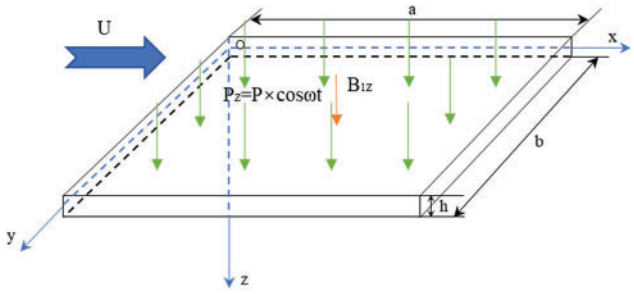

Figure 1: Rectangular conductive thin plate model under the combined action of subsonic airflow and periodic excitation in a magnetic field

The research idea of this paper is shown in Fig. 2 below.

2.1 Four Basic Conditional Assumptions of Thin Plate Theory

When studying the lateral vibration of elastic thin plates, there are four basic assumptions [30]:

(1) The vertical line segment perpendicular to the mid-plane of the thin plate has no change in its properties and is perpendicular to the deformed mid-plane.

(2) The layers of materials parallel to the middle surface do not have mutual extrusion.

(3) When the plate is bent, the amount of deflection in the z direction changes to zero.

(4) When the plate is bent, there is no expansion and shear deformation at each point in the middle plane of the plate.

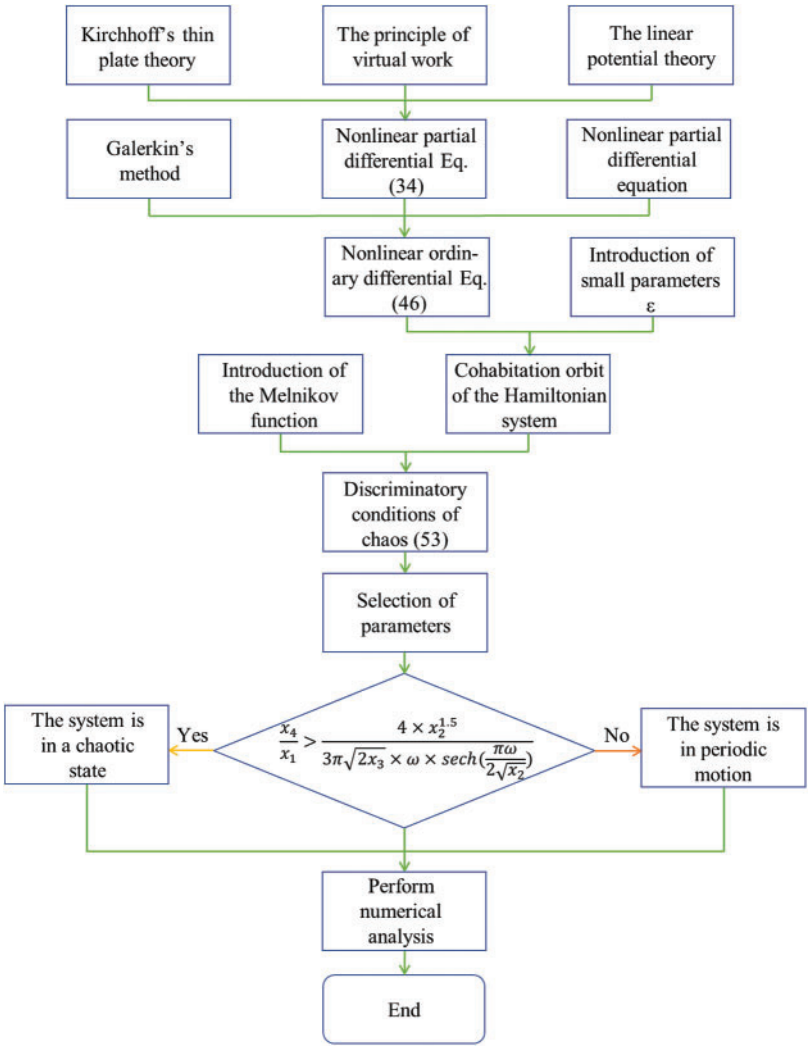

Figure 2: Flow chart of the article's expository ideas

2.2 Stress Strain Relationship

According to the elastic deformation theory, when the plate moves, the displacement of each point whose internal distance is z from the mid-plane can be expressed as follows:

$$\begin{cases} u_x = u(x, y, t) + z\vartheta_x(x, y, t) \\ u_y = v(x, y, t) + z\vartheta_y(x, y, t) \\ u_z = w(x, y, t) \end{cases} \tag{1}$$

In Eq. (1), u, v, w are the displacement components of the points in the midplane, t denotes time, and u_x, u_y, u_z are the displacement components in the x, y and z directions, respectively. $\vartheta_x = -\frac{\partial w}{\partial x}$, $\vartheta_y = -\frac{\partial w}{\partial y}$.

According to the assumption of the Kirchhoff straight line method, $\varepsilon_{xz} = \varepsilon_{yz} = \varepsilon_{zz} = 0$, the strain component of the displacement of the midplane of the plate can be obtained as:

$$\begin{cases} \varepsilon_{xx} = \varepsilon_x + z\kappa_x \\ \varepsilon_{yy} = \varepsilon_y + z\kappa_y \\ \varepsilon_{xy} = \xi + z\kappa_{xy} \end{cases} \tag{2}$$

In Eq. (2), $\varepsilon_x = \dfrac{\partial u}{\partial x} + \dfrac{1}{2}\left(\dfrac{\partial w}{\partial x}\right)^2$, $\varepsilon_y = \dfrac{\partial v}{\partial y} + \dfrac{1}{2}\left(\dfrac{\partial w}{\partial y}\right)^2$, $\xi = \dfrac{\partial v}{\partial x} + \dfrac{\partial u}{\partial y} + \dfrac{\partial w}{\partial x}\dfrac{\partial w}{\partial y}$, $\kappa_x = -\dfrac{\partial^2 w}{\partial x^2}$, $\kappa_y = -\dfrac{\partial^2 w}{\partial y^2}$, $\kappa_{xy} = -\dfrac{\partial^2 w}{\partial x \partial y}$.

where κ_x and κ_y are the curvature, κ_{xy} is the twist rate, and ε_x, ε_y and ξ are the strain components.

According to the basic assumption of Kirchhoff, using the generalized Hooke's law [30], the stress can be described as:

$$\begin{cases} \sigma_{xx} = \dfrac{E}{1-\mu^2}\left(\varepsilon_{xx} + \mu\varepsilon_{xy}\right) \\ \sigma_{yy} = \dfrac{E}{1-\mu^2}\left(\varepsilon_{yy} + \mu\varepsilon_{xx}\right) \\ \sigma_{xy} = \sigma_{yx} = \dfrac{E}{2\left(1+\mu\right)}\varepsilon_{xy} \end{cases} \tag{3}$$

In Eq. (3), E is the Young's modulus of the material, and μ is the Poisson's ratio. The equation for large deflection bending of the plate can be obtained as:

$$N_x = \int_{-\frac{h}{2}}^{\frac{h}{2}} \sigma_{xx} dz = D_N\left(\varepsilon_x + \mu\varepsilon_y\right) \tag{4}$$

$$N_y = \int_{-\frac{h}{2}}^{\frac{h}{2}} \sigma_{yy} dz = D_N\left(\varepsilon_y + \mu\varepsilon_x\right) \tag{5}$$

$$N_{xy} = \int_{-\frac{h}{2}}^{\frac{h}{2}} \sigma_{xy} dz = D_N \frac{1-\mu}{2}\xi \tag{6}$$

$$M_x = \int_{-\frac{h}{2}}^{\frac{h}{2}} \sigma_{xx} z dz = D_M\left(\kappa_x + \mu\kappa_y\right) \tag{7}$$

$$M_y = \int_{-\frac{h}{2}}^{\frac{h}{2}} \sigma_{yy} z dz = D_M\left(\kappa_y + \mu\kappa_x\right) \tag{8}$$

$$M_{xy} = \int_{-\frac{h}{2}}^{\frac{h}{2}} \sigma_{xy} z dz = D_M\left(1-\mu\right)\kappa_{xy} \tag{9}$$

In Eqs. (4)–(9), M_x, M_y is bending moment, N_x, N_y, N_{xy} represent internal force, M_{xy} is torque, D_N is tensile stiffness, D_M is flexural rigidity.

2.3 Preliminary Establishment of Partial Differential Equations of Motion

During the imaginary displacement, the increment of deformation potential energy of the plate is:

$$\delta U = \int\int_{\Sigma}\left[\int_{\frac{-h}{2}}^{\frac{h}{2}} \sigma_{xx}\delta\varepsilon_{xx} + \sigma_{yy}\delta\varepsilon_{yy} + \sigma_{xy}\delta\varepsilon_{xy}dz\right]dxdy \tag{10}$$

The imaginary work done by the external force on the imaginary displacement is:

$$\begin{aligned}\delta W = \int\int_{\Sigma}\Bigg[&\left(F_x - \Delta P_x + P_x - \rho\frac{\partial^2 u}{\partial t^2}\right)\delta u + \left(F_y - \Delta P_y + P_y - \rho\frac{\partial^2 v}{\partial t^2}\right)\delta v \\ &+ \left(F_z - \Delta P_z + P_z - \rho\frac{\partial^2 w}{\partial t^2}\right)\delta w + \left(m_x - \frac{\rho h^3}{12}\frac{\partial^2\vartheta_x}{\partial t^2}\right)\delta\vartheta_x + \left(m_y - \frac{\rho h^3}{12}\frac{\partial^2\vartheta_y}{\partial t^2}\right)\delta\vartheta_y\Bigg]dxdy\end{aligned} \tag{11}$$

According to the principle of virtual displacement, the condition for the system to remain stationary is the external force acting on the system, and the sum of the virtual work done on the virtual displacement and the system deformation potential energy is zero [31], namely:

$$\delta U = \delta W \tag{12}$$

According to Kirchhoff's theory, considering the coupling effect of the thin plate under the external excitation and the electromagnetic field, using the principle of virtual work, the following magnetoelastic equation can be obtained as [16]:

$$\frac{\partial N_x}{\partial x} + \frac{\partial N_{xy}}{\partial y} + F_x - \Delta P_x + P_x = \rho h\frac{\partial^2 u}{\partial t^2} \tag{13}$$

$$\frac{\partial N_y}{\partial y} + \frac{\partial N_{xy}}{\partial x} + F_y - \Delta P_y + P_y = \rho h\frac{\partial^2 v}{\partial t^2} \tag{14}$$

$$\begin{aligned}&\frac{\partial^2 M_x}{\partial x^2} + \frac{\partial^2 M_y}{\partial y^2} + 2\frac{\partial^2 M_{xy}}{\partial x\partial y} + \frac{\partial}{\partial x}\left(N_x\frac{\partial w}{\partial x} + N_{xy}\frac{\partial w}{\partial y}\right) + \frac{\partial}{\partial y}\left(N_y\frac{\partial w}{\partial y} + N_{xy}\frac{\partial w}{\partial x}\right) \\ &+ \frac{\partial m_x}{\partial x} + \frac{\partial m_y}{\partial y} + F_z - \Delta P_z + P_z = \rho h\frac{\partial^2 w}{\partial t^2} - \frac{\rho h^3}{12}\frac{\partial^2\left(\nabla^2 w\right)}{\partial t^2}\end{aligned} \tag{15}$$

In Eqs. (11)–(15), ΔP_x, ΔP_y, ΔP_z represent subsonic aerodynamic force, P_x, P_y, P_z represent mechanical surface force that are simplified to the mid-plane, F_x, F_y, F_z represent the electromagnetic force, m_x, m_y represent the electromagnetic moment, ρ is the density of the rectangular thin plate.

2.4 Derivation of Basic Theory of Electromagnetic Field

Assuming that the thin plate is a non-polarized, non-magnetized material with good conductivity, the electromagnetic quantity satisfies the Maxwell equation [13]:

$$\begin{cases}\nabla \boldsymbol{D} = 0 \\ \nabla \boldsymbol{B} = 0 \\ \nabla \boldsymbol{E} = -\dfrac{\partial \boldsymbol{B}}{\partial t} \\ \nabla \boldsymbol{H} = \boldsymbol{J} + \dfrac{\partial \boldsymbol{D}}{\partial t}\end{cases} \tag{16}$$

The electromagnetic constitutive relation is as follows:

$$\begin{cases} \boldsymbol{D} = \varepsilon_0 \boldsymbol{E} \\ \boldsymbol{B} = \mu_0 \boldsymbol{H} \\ \boldsymbol{J} = \varrho \left(\boldsymbol{E} + \dfrac{\partial \boldsymbol{u}}{\partial t} \boldsymbol{B} \right) \end{cases} \tag{17}$$

In Eqs. (16) and (17), $\boldsymbol{H}$ is the magnetic field strength, $\boldsymbol{B}$ is the magnetic flux density, $\boldsymbol{J}$ is the current density, $\boldsymbol{E}$ is the electric field strength, $\boldsymbol{D}$ is the electric flux density, u is the point displacement, ε_0 is the permittivity, ϱ is the electrical conductivity, μ_0 is the magnetic permeability, $\nabla = \boldsymbol{i}\dfrac{\partial}{\partial x} + \boldsymbol{j}\dfrac{\partial}{\partial y} + \boldsymbol{k}\dfrac{\partial}{\partial z}$, $\boldsymbol{i}, \boldsymbol{j}, \boldsymbol{k}$ are unit vectors.

When it is in the motion state under the magnetic field, the electromagnetic quantity in the thin plate can be written as:

$$\boldsymbol{H} = \boldsymbol{H}_1 \left(H_{1x}, H_{1y}, H_{1z} \right) + \boldsymbol{h} \left(h_x, h_y, h_z \right) \tag{18}$$

$$\boldsymbol{B} = \boldsymbol{B}_1 \left(B_{1x}, B_{1y}, B_{1z} \right) + \boldsymbol{b} \left(b_x, b_y, b_z \right) \tag{19}$$

$$\boldsymbol{E} = \boldsymbol{e} \left(e_x, e_y, e_z \right) \tag{20}$$

$$\boldsymbol{D} = \boldsymbol{d} \left(d_x, d_y, d_z \right) \tag{21}$$

In Eqs. (18)–(21), $\boldsymbol{H}_1$ and $\boldsymbol{B}_1$ are the magnetic field distributions under the initial condition of the thin plate; $\boldsymbol{h}$, $\boldsymbol{b}$, $\boldsymbol{e}$, $\boldsymbol{d}$ are the electromagnetic vectors generated after being excited.

From the Eq. (17), the in-plane induced current can be obtained as:

$$J_x = \varrho \left(e_x - \frac{\partial u_z}{\partial t} B_{1y} + B_{1z} \left(\frac{\partial u_y}{\partial t} + z \frac{\partial \vartheta_y}{\partial t} \right) \right) \tag{22}$$

$$J_y = \varrho \left(e_y + \frac{\partial u_z}{\partial t} B_{1x} - B_{1z} \left(\frac{\partial u_x}{\partial t} + z \frac{\partial \vartheta_x}{\partial t} \right) \right) \tag{23}$$

$$J_z = 0 \tag{24}$$

2.5 Differential Equation of Motion of Rectangular Thin Plate under External Excitation in Transverse Magnetic Field

The vector expression of the Lorenz force acting on a deformed object by an electromagnetic field is:

$$\boldsymbol{f} = \boldsymbol{JB} = \begin{vmatrix} \boldsymbol{i} & \boldsymbol{j} & \boldsymbol{k} \\ J_x & J_y & o \\ B_{1x} & B_{1y} & B_{1z} \end{vmatrix} \tag{25}$$

The unit volume electromagnetic force is:

$$f_x = \varrho B_{1z} \left(e_y + B_{1x} \frac{\partial w}{\partial t} - B_{1z} \left(\frac{\partial u}{\partial t} - z \frac{\partial^2 w}{\partial t \partial x} \right) \right) \tag{26}$$

$$f_y = -\varrho B_{1z}\left(e_x - B_{1y}\frac{\partial w}{\partial t} + B_{1z}\left(\frac{\partial v}{\partial t} - z\frac{\partial^2 w}{\partial t \partial x}\right)\right) \tag{27}$$

$$f_z = \varrho B_{1z}\left(e_y + \frac{\partial w}{\partial t} - B_{1z}\left(\frac{\partial u}{\partial t} - z\frac{\partial^2 w}{\partial t \partial x}\right)\right) \tag{28}$$

Integrating Eqs. (26)–(28) in z from $-\frac{h}{2}$ to $\frac{h}{2}$, when there is only a transverse magnetic field, the electromagnetic force and electromagnetic torque on the unit area of the thin plate:

$$F_x = \int_{-\frac{h}{2}}^{\frac{h}{2}} f_x dz = \varrho h B_{1z}\left(e_y - B_{1z}\frac{\partial u}{\partial t}\right) \tag{29}$$

$$F_y = \int_{-\frac{h}{2}}^{\frac{h}{2}} f_y dz = -\varrho h B_{1z}\left(e_x - B_{1z}\frac{\partial v}{\partial t}\right) \tag{30}$$

$$F_z = 0 \tag{31}$$

$$m_x = \int_{-\frac{h}{2}}^{\frac{h}{2}} f_x z dz = \frac{\varrho h^3}{12} {B_{1z}}^2 \frac{\partial^2 w}{\partial t \partial x} \tag{32}$$

$$m_y = \int_{-\frac{h}{2}}^{\frac{h}{2}} f_y z dz = \frac{\varrho h^3}{12} {B_{1z}}^2 \frac{\partial^2 w}{\partial t \partial y} \tag{33}$$

Substituting Eqs. (29)–(33) and the corresponding equation into Eqs. (13)–(15), considering the existence of lateral deformation and damping, the following partial differential equation of motion of a rectangular thin plate in a transverse magnetic field environment can be obtained [15]:

$$\rho h \ddot{w} + D_M \nabla^4 w - \frac{1}{2} D_N \left[3\left(\frac{\partial w}{\partial x}\right)^2 \frac{\partial^2 w}{\partial x^2} + 3\left(\frac{\partial w}{\partial y}\right)^2 \frac{\partial^2 w}{\partial y^2} + \frac{\partial^2 w}{\partial x^2}\left(\frac{\partial w}{\partial y}\right)^2 + \left(\frac{\partial w}{\partial x}\right)^2 \frac{\partial^2 w}{\partial y^2} + 4\frac{\partial w}{\partial x}\frac{\partial w}{\partial y}\frac{\partial^2 w}{\partial x \partial y}\right] - \frac{\varrho h^3}{12} B_{1z}^2 \frac{\partial}{\partial t}\left(\frac{\partial^2 w}{\partial x^2} + \frac{\partial^2 w}{\partial y^2}\right) + c\dot{w} + R_z = 0 \tag{34}$$

$$R_z = \Delta P_z - P\cos\omega t \tag{35}$$

$$\nabla^4 = \frac{\partial^4}{\partial x^4} + 2\frac{\partial^4}{\partial x^2 \partial y^2} + \frac{\partial^4}{\partial y^4} \tag{36}$$

In Eqs. (34)–(36), ρ is the density of the rectangular thin plate; c is the structural damping coefficient; B_{1z} is the magnetic field distribution; ∇^4 is the Double Laplace operator; ΔP_z is subsonic aerodynamic force; ϱ is electrical conductivity; ω denotes the intrinsic frequency of the mechanical surface force.

From the simply supported condition of the four sides of the rectangular thin plate, the method of separation of variables [22,32] is adopted, and the lateral displacement is given as:

$$w = \varphi_{i,j}(x, y)\, q_{i,j}(t) \tag{37}$$

Using the mode shape superposition method, the solution $\varphi(x,y)$ of the mode shape equation satisfying this boundary condition is set to:

$$\varphi_{i,j}(x,y) = \sin\frac{i\pi x}{a}\sin\frac{j\pi y}{b} \quad (i,j = 1,2,\ldots) \tag{38}$$

In the above equations, $\varphi(x,y)$ is the mode shape, $q(t)$ is the generalized coordinate, only the first-order mode is considered here.

According to the linear potential theory [1,33], the pneumatic pressure ΔP is obtained as:

$$\Delta P = \frac{ab\rho_\Delta}{\pi\sqrt{a^2+b^2}}\left[\varphi\ddot{q} + 2U\frac{\partial\varphi}{\partial x}\dot{q} + U^2\frac{\partial^2\varphi}{\partial x^2}q\right] \tag{39}$$

Substitute Eqs. (35), (36), (38), (39) into Eq. (34), and use Galerkin's method to integrate [34], the ordinary differential equation is obtained:

$$s_1\ddot{q} + s_2\dot{q} - s_3 q + s_4 q^3 = P_0\cos\omega t \tag{40}$$

The parameters s_1, s_2, s_3, s_4, P_0 in Eq. (40) are:

$$s_1 = \int_0^b\int_0^a\left(\rho h + \frac{ab\rho_\Delta}{\pi\sqrt{a^2+b^2}}\right)\varphi^2 dxdy = \frac{a^2b^2\rho_\Delta}{4\sqrt{a^2+b^2}\pi} + \frac{1}{4}abh\rho \tag{41}$$

$$\begin{aligned} s_2 &= \int_0^b\int_0^a\left[c\varphi^2 + \frac{2ab\rho_\Delta U\varphi}{\pi\sqrt{a^2+b^2}}\frac{\partial\varphi}{\partial x} - \frac{\varrho h^3\varphi}{12}B_{1z}^2\left(\frac{\partial^2\varphi}{\partial x^2} + \frac{\partial^2\varphi}{\partial y^2}\right)\right]dxdy \\ &= \frac{abc}{4} - \frac{aB_{1z}^2h^3\varrho\pi^2}{48b} - \frac{bB_{1z}^2h^3\varrho\pi^2}{48a} \end{aligned} \tag{42}$$

$$\begin{aligned} s_3 &= \int_0^b\int_0^a\left(\frac{U^2ab\rho_\Delta}{\pi\sqrt{a^2+b^2}}\frac{\partial^2\varphi}{\partial x^2} - D_M\left(\frac{\partial^4\varphi}{\partial x^4} + \frac{\partial^4\varphi}{\partial y^4} + 2\frac{\partial^4\varphi}{\partial x^2\partial y^2}\right)\right)\varphi dxdy \\ &= \frac{b^2\rho_\Delta\pi\,U_\Delta{}^2}{4\sqrt{a^2+b^2}} - D_M\left(\frac{a\pi^4}{4b^3} + \frac{\pi^4}{2ab} + \frac{b\pi^4}{4a^3}\right) \end{aligned} \tag{43}$$

$$\begin{aligned} s_4 = -\frac{1}{2}D_N\int_0^b\int_0^a\Bigg[&3\left(\frac{\partial\varphi}{\partial x}\right)^2\frac{\partial^2\varphi}{\partial x^2} + 3\left(\frac{\partial\varphi}{\partial y}\right)^2\frac{\partial^2\varphi}{\partial y^2} + \frac{\partial^2\varphi}{\partial x^2}\left(\frac{\partial\varphi}{\partial y}\right)^2 + \frac{\partial^2\varphi}{\partial y^2}\left(\frac{\partial\varphi}{\partial x}\right)^2 \\ &+ 4\frac{\partial\varphi}{\partial x}\frac{\partial\varphi}{\partial y}\frac{\partial^2\varphi}{\partial x\partial y}\Bigg]\varphi dxdy = D_N\left(\frac{9a\pi^4}{128b^3} + \frac{\pi^4}{64ab} + \frac{9b\pi^4}{128a^3}\right) \end{aligned} \tag{44}$$

$$P_0 = \int_0^b\int_0^a P\varphi dxdy = \frac{4abP}{\pi^2} \tag{45}$$

3 Nonlinear Motion Analysis

3.1 Geometry Structure

Let $x_1 = s_2/s_1$, $x_2 = s_3/s_1$, $x_3 = s_4/s_1$, $x_4 = P_0/s_1$, then the Eq. (40) translates into:

$$\ddot{q} + x_1\dot{q} - x_2 q + x_3 q^3 = x_4\cos\omega t \tag{46}$$

The damping coefficient and the force coefficient are considered as perturbation terms. Introducing the small parameter ε, rewrite the equation as [33]:

$$\begin{cases} \dot{q} = z \\ \dot{z} = x_2 q - x_3 q^3 + \varepsilon \left(\overline{x_4} \cos \omega t - \overline{x_1} z \right) \end{cases} \tag{47}$$

where $\overline{x_4} = \dfrac{x_4}{\varepsilon}$, $\overline{x_1} = \dfrac{x_1}{\varepsilon}$.

Assuming $\varepsilon = 0$, the corresponding undisturbed Hamilton system is [35]:

$$\begin{cases} \dot{q} = z \\ \dot{z} = x_2 q - x_3 q^3 \end{cases} \tag{48}$$

Let $\dot{q} = \dot{z} = 0$, three fixed points can be obtained: $O\ (0,0)$; $A\left(\sqrt{\dfrac{x_2}{x_3}}, 0\right)$; $B\left(-\sqrt{\dfrac{x_2}{x_3}}, 0\right)$. The Hamilton function of the system is:

$$H(q,z) = \frac{1}{2} z^2 - \frac{1}{2} x_2 q^2 + \frac{1}{4} x_3 q^4 \tag{49}$$

A hyperbolic saddle point in the q-z plane and two homoclinic orbits [36]:

$$\left(q^+(t), z^+(t)\right) = \left(\frac{3x_2}{\sqrt{\dfrac{9}{2} x_2 x_3} \times \cosh\left(\sqrt{x_2} t\right)}, \sqrt{\frac{2}{x_3}} x_2 \operatorname{sech}\left(\sqrt{x_2} t\right) tanh\left(\sqrt{x_2} t\right) \right) \tag{50}$$

$$\left(q^-(t), z^-(t)\right) = \left(\frac{-3x_2}{\sqrt{\dfrac{9}{2} x_2 x_3} \times \cosh\left(\sqrt{x_2} t\right)}, -\sqrt{\frac{2}{x_3}} x_2 sech\left(\sqrt{x_2} t\right) tanh\left(\sqrt{x_2} t\right) \right) \tag{51}$$

3.2 Necessary Conditions for Chaos to Exist

When ε is small enough, the still existing hyperbolic invariant torus of the Hamilton system that is subject to the tiny attraction can be judged whether the stable and unstable manifolds intersect or not according to the extended Melnikov function [37,38].

The generalized Melnikov function $M(t_0)$ [37] given by the Eq. (48) is:

$$M(t_0) = \int_{-\infty}^{+\infty} -x_1 [z^{\pm}(t)]^2 + x_4 [\cos(\omega (t - t_0)] z^{\pm}(t)\, dt \tag{52}$$

If the Melnikov function has only one simple zero, the Poincaré map of the disturbance system Eq. (48) has a Strange Attractor, and chaotic motion is possible.

With the continuous increase of x_4/x_1, the stable and unstable manifolds of the system will gradually intersect, which leads to the generation of chaotic motion in the sense of Smale horseshoe [39]. Therefore let $M(t_0) = 0$, it can be deduced that the necessary condition for the existence of chaos in the system is:

$$\frac{\overline{x_4}}{\overline{x_1}} = \frac{\dfrac{x_4}{\varepsilon}}{\dfrac{x_1}{\varepsilon}} = \frac{x_4}{x_1} > \frac{4 \times x_2^{1.5}}{3\pi \sqrt{2x_3} \times \omega \times \operatorname{sech}\left(\dfrac{\pi \omega}{2\sqrt{x_2}}\right)} \tag{53}$$

4 Results and Analysis of Example

Numerical simulations are performed using MATLAB software, and the Four-Order Range-Kuttle Method is used for iterative calculations to obtain the bifurcation diagram, phase portrait, Poincaré map and time history response of the system.

The structure and material parameters are selected as: $a = 1.5$ m, $b = 1.0$ m, $h = 0.002$ m, $\rho = 2500$ kg/m^3, $\rho_\Delta = 1.29$ kg/m^3, $E = 7\times10^{10}$ N/m^2, $\mu = 0.3$, $c = 25$ N$\cdot$(m $\cdot$ s^{-1}), $\varrho = 3.6\times10^7$ $(\Omega \cdot \mathrm{m})^{-1}$.

The surface corresponding to $x_4/x_1 = 2\sqrt{2} \times x_2^{1.5}/\left\{3\pi\sqrt{x_3}\left[\omega \times \operatorname{csch}\left(\omega\pi/2\sqrt{x_2}\right)\right]\right\}$ is a critical surface, and only when x_4/x_1 is located above the critical surface, the chaotic motion can meet the conditions for generating.

The motion of the system discussed in this paper is affected by two changing factors, that is, the magnetic field distribution B_{1z} and the incoming velocity U. Taking the magnetic field distribution B_{1z} as $0T$, $5T$, and $7.5T$, respectively, and discussing the motion behavior of the system.

4.1 When the Magnetic Field Distribution $B_{1z} = 0T$

Selecting $x_4/x_1 = 6.405$, $\omega = 20$ rad/s, Fig. 3 is the bifurcation diagram of the relationship between the displacement of the mid-point of the plate and the incoming velocity U. As can be seen from Fig. 3, periodic vibration and chaotic motion appear alternately.

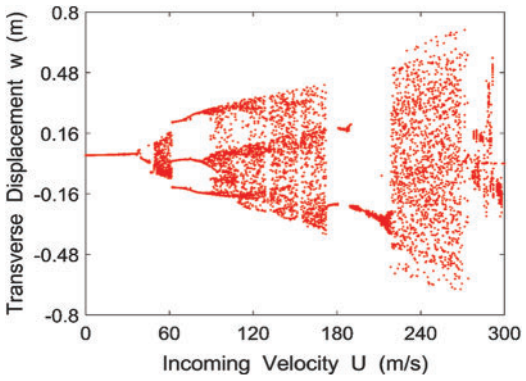

Figure 3: Bifurcation diagram of the lateral displacement of the midpoint of the rectangular conductive thin plate with respect to the incoming velocity

Take $U = 100$ m/s, $U = 150$ m/s, $U = 200$ m/s, and $U = 250$ m/s into Eq. (53), respectively. When $U = 100$ m/s, $2\sqrt{2} \times x_2^{1.5}/\left\{3\pi\sqrt{x_3}\left[\omega \times \operatorname{csch}\left(\omega\pi/2\sqrt{x_2}\right)\right]\right\} = 0.015 < x_4/x_1 = 6.405$, satisfying the discriminant condition for the existence of chaos. When $U = 150$ m/s, $2\sqrt{2} \times x_2^{1.5}/\left\{3\pi\sqrt{x_3}\left[\omega \times \operatorname{csch}\left(\omega\pi/2\sqrt{x_2}\right)\right]\right\} = 0.067 < x_4/x_1 = 6.405$, satisfying the discriminant condition for the existence of chaos. When $U = 200$ m/s, $2\sqrt{2}\times x_2^{1.5}/\left\{3\pi\sqrt{x_3}\left[\omega \times \operatorname{csch}\left(\omega\pi/2\sqrt{x_2}\right)\right]\right\} = 0.139 < x_4/x_1 = 6.405$, satisfying the discriminant condition for the existence of chaos. When $U = 250$ m/s, $2\sqrt{2} \times x_2^{1.5}/\left\{3\pi\sqrt{x_3}\left[\omega \times \operatorname{csch}\left(\omega\pi/2\sqrt{x_2}\right)\right]\right\} = 0.231 < x_4/x_1 = 6.405$, satisfying the discriminant condition for the existence of chaos. From this, the time history response, phase portrait and Poincaré map of the system are drawn.

The time history response for the four cases of $U = 100$ m/s, $U = 150$ m/s, $U = 200$ m/s, and $U = 250$ m/s, are shown in Figs. 4a–4d. As can be seen from Fig. 4, the time history response of the system has no periodicity at all, which indicates that the motion of the system presents a chaotic nature

at this time. When the magnetic field strength is 0T (constant magnetic field strength), the incoming velocity affects the amplitude of the system vibration as well as the stability of the motion. When the incoming velocity $U = 200$ m/s, the system is more stable compared to the other three cases, which can also be seen in Fig. 3, when the scatter distribution of the bifurcation diagram of the system is relatively less.

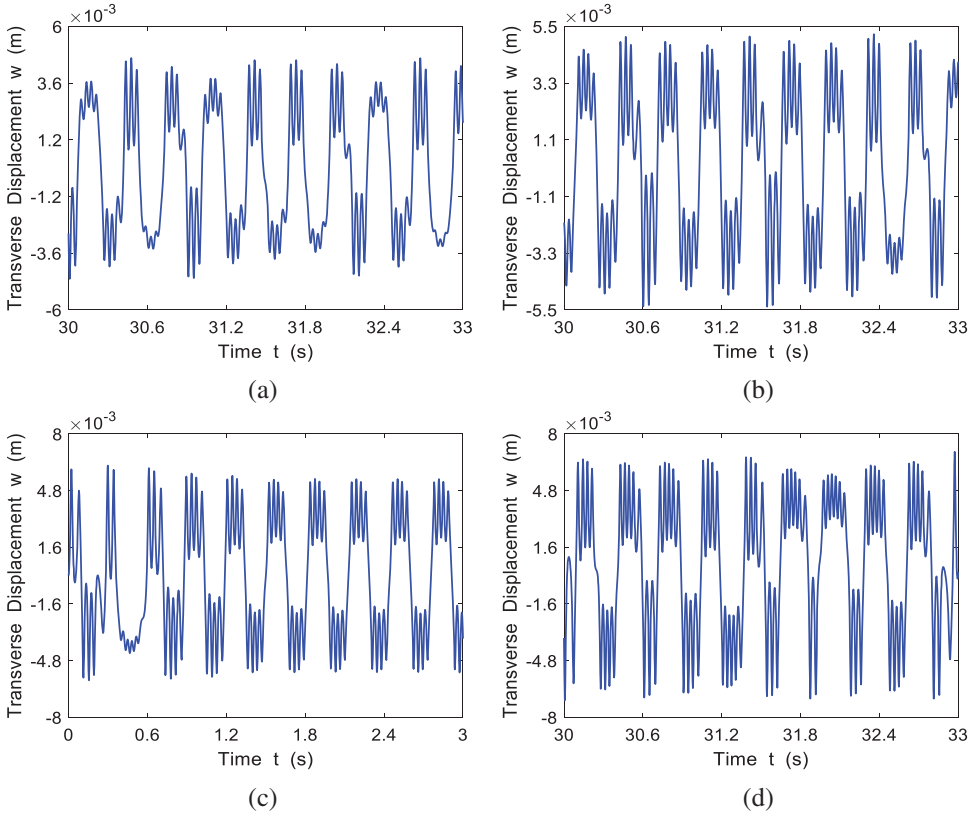

Figure 4: The time history response of the system at different incoming velocities

The phase portrait for the four cases of $U = 100$ m/s, $U = 150$ m/s, $U = 200$ m/s, and $U = 250$ m/s, are shown in Figs. 5a–5d. As can be seen from Fig. 5, there are many unclosed limit cycles in the phase portrait of the system, which are restricted to a bounded region, which indicates that the motion of the system presents a chaotic nature at this time. Compared with the other three cases, the number of limit cycles in the phase portrait of the system is relatively less when the incoming velocity $U = 200\ m/s$, which also indicates that the motion of the system is relatively the most stable at this time. This is consistent with the case of the time history response shown in Fig. 4.

The Poincaré map for the four cases of $U = 100$ m/s, $U = 150$ m/s, $U = 200$ m/s, and $U = 250$ m/s, are shown in Figs. 6a–6d. As can be seen from the Poincaré map, there is a fractal structure of dense points in the cross section, which is neither a finite set of points nor a closed curve, which indicates that the motion of the system at this time presents a chaotic state. The scatter distribution in Fig. 6c is relatively small, while the scatter distribution in Figs. 6a–6d are relatively denser and presents a more perfect Poincaré map of the Duffing system in the chaotic state. The bifurcation diagram of the system can also reflect this situation, the number of scatter points in this case is relatively smaller.

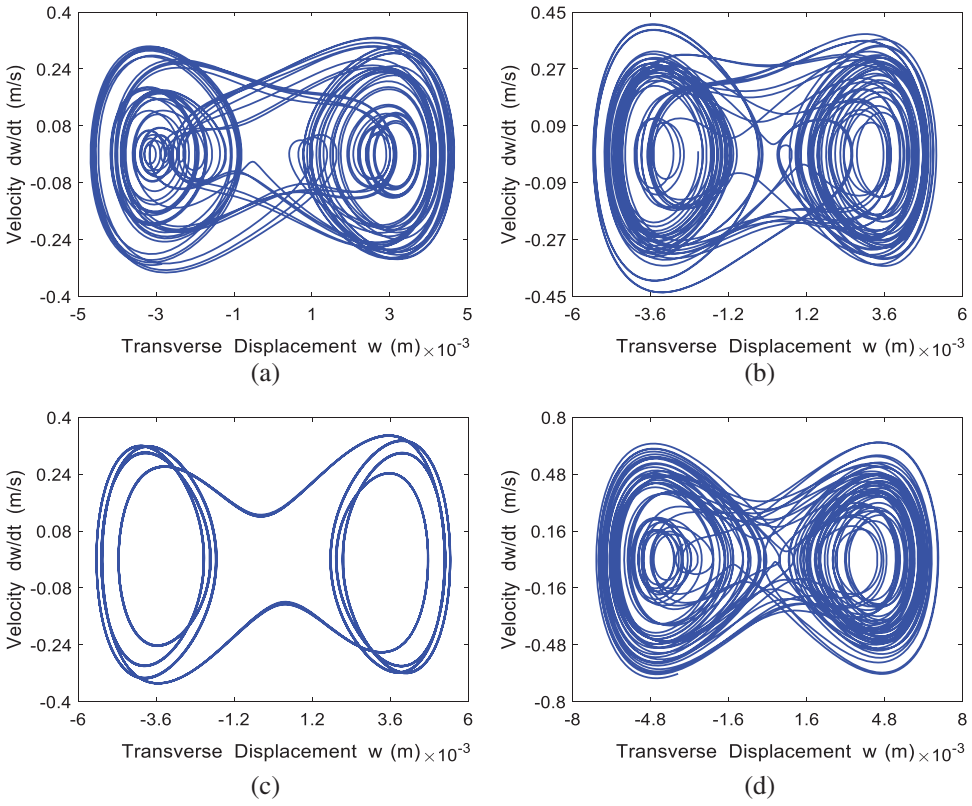

Figure 5: The phase portrait of the system at different incoming velocities

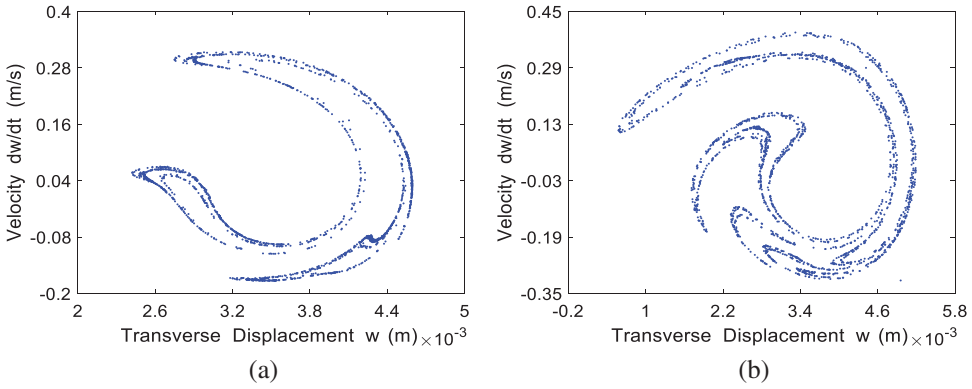

Figure 6: (Continued)

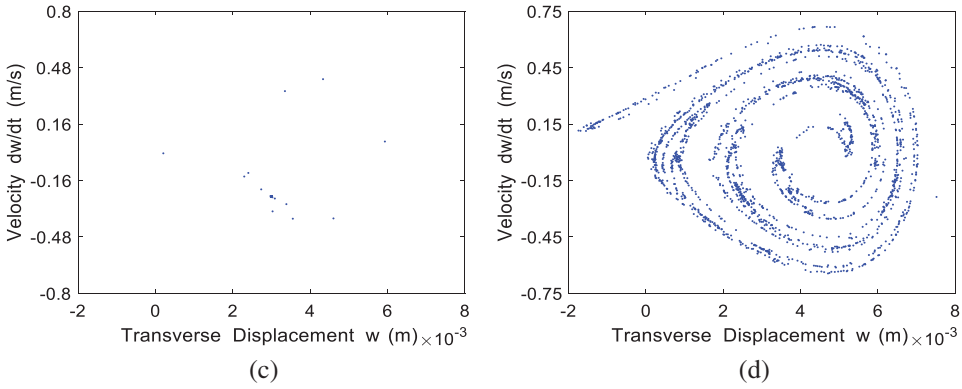

Figure 6: The Poincaré map of the system at different incoming velocities

4.2 When the Magnetic Field Distribution $B_{1z} = 5T$

Selecting $x_4/x_1 = 9.73$, $\omega = 20$ rad/s, Fig. 7 is the bifurcation diagram of the relationship between the displacement of the mid-point of the plate and the incoming velocity U. As can be seen from Fig. 7, periodic vibration and chaotic motion appear alternately. Compared to Fig. 3, the region of multiply periodic motion is reduced in Fig. 7. This indicates that the chaotic region of the system has changed and the stability of the system has decreased due to the intervention of the magnetic field.

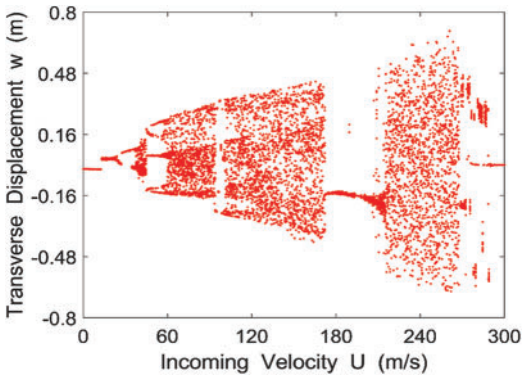

Figure 7: Bifurcation diagram of the lateral displacement of the midpoint of the rectangular conductive thin plate with respect to the incoming velocity

Take $U = 100$ m/s, $U = 150$ m/s, $U = 200$ m/s, and $U = 250$ m/s into Eq. (53), respectively. When $U = 100$ m/s, $2\sqrt{2} \times x_2^{1.5}/3\pi\sqrt{x_3}\left[\omega \times \operatorname{csch}\left(\omega\pi/2\sqrt{x_2}\right)\right] = 0.015 < x_4/x_1 = 9.73$, satisfying the discriminant condition for the existence of chaos. When $U = 150$ m/s, $2\sqrt{2} \times x_2^{1.5}/3\pi\sqrt{x_3}\left[\omega \times \operatorname{csch}\left(\omega\pi/2\sqrt{x_2}\right)\right] = 0.067 < x_4/x_1 = 9.73$, satisfying the discriminant condition for the existence of chaos. When $U = 200$ m/s, $2\sqrt{2} \times x_2^{1.5}/3\pi\sqrt{x_3}\left[\omega \times \operatorname{csch}\left(\omega\pi/2\sqrt{x_2}\right)\right] = 0.139 < x_4/x_1 = 9.73$, satisfying the discriminant condition for the existence of chaos. When $U = 250$ m/s, $2\sqrt{2} \times x_2^{1.5}/3\pi\sqrt{x_3}\left[\omega \times \operatorname{csch}\left(\omega\pi/2\sqrt{x_2}\right)\right] = 0.231 < x_4/x_1 = 9.73$, satisfying the discriminant condition for the existence of chaos. From this, the time history response, phase portrait and Poincaré map of the system are drawn. The change in magnetic field only changes the value of x_4/x_1 and does not affect the value of $2\sqrt{2} \times x_2^{1.5}/3\pi\sqrt{x_3}\left[\omega \times \operatorname{csch}\left(\omega\pi/2\sqrt{x_2}\right)\right]$. Even if there are different magnetic field distributions, the critical surface remains the same if the incoming velocity is constant. The presence

of the magnetic field further expands the chaotic region of the system, in which the magnetic field also acts as a damping agent.

The time history response for the four cases of $U = 100$ m/s, $U = 150$ m/s, $U = 200$ m/s, and $U = 250$ m/s are shown in Figs. 8a–8d. As can be seen from Fig. 8, the time history response of the system has no periodicity at all, which indicates that the motion of the system presents a chaotic nature at this time. When the magnetic field strength is 5T (constant magnetic field strength), the incoming velocity affects the amplitude of the system vibration as well as the stability of the motion. When the incoming velocity $U = 200$ m/s, the system is more stable compared to the other three cases. This can also be seen in Fig. 7, where the scatter distribution of the bifurcation diagram of the system is relatively small at this point. Compared to Fig. 4, the stability exhibited in Fig. 8 has decreased, which is related to the expansion of the chaotic region of the system.

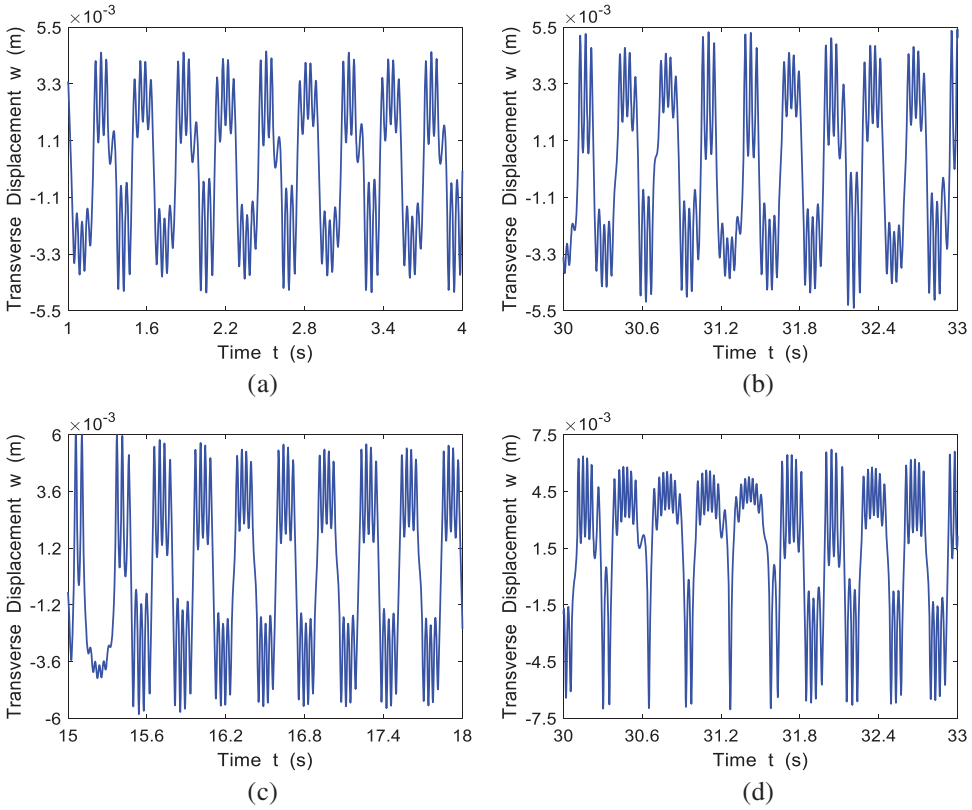

Figure 8: The time history response of the system at different incoming velocities

The phase portrait for the four cases of $U = 100$ m/s, $U = 150$ m/s, $U = 200$ m/s, and $U = 250$ m/s are shown in Figs. 9a–9d. As can be seen from Fig. 9, there are many unclosed limit cycles in the phase portrait of the system, which are restricted to a bounded region, which indicates that the motion of the system presents a chaotic nature at this time. Compared with the other three cases, the number of limit cycles in the phase portrait of the system is relatively less when the incoming velocity $U = 200$ m/s, which also indicates that the motion of the system is relatively the most stable at this time. This is consistent with the case of the time history response shown in Fig. 8.

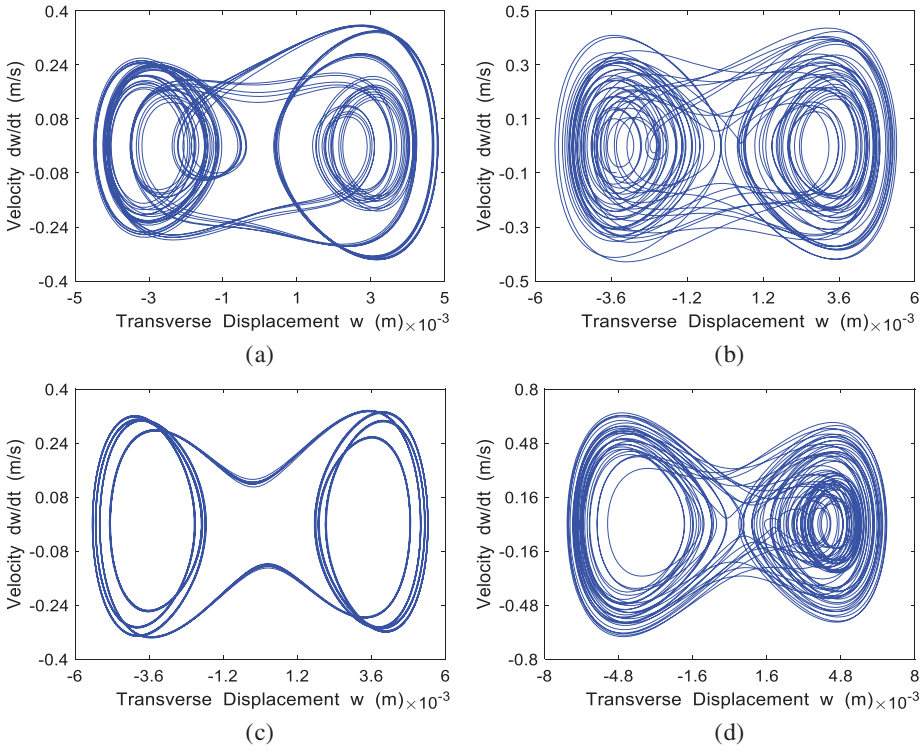

Figure 9: The phase portrait of the system at different incoming velocities

The Poincaré map for the four cases of $U = 100$ m/s, $U = 150$ m/s, $U = 200$ m/s, and $U = 250$ m/s are shown in Figs. 10a–10d. As can be seen from the Poincaré map, there is a fractal structure of dense points in the cross section, which is neither a finite set of points nor a closed curve, which indicates that the motion of the system at this time presents a chaotic state. The scatter distribution in Fig. 10c is relatively small, while the scatter distribution in Figs. 10a–10d is relatively denser and presents a more perfect Poincaré map of the Duffing system in the chaotic state. The bifurcation diagram of the system can also reflect this situation, the number of scatter points in this case is relatively smaller. However, compared to Fig. 6c, there are a larger number of scatter points in Fig. 10c, which is a result of the expansion of the chaotic region of the system.

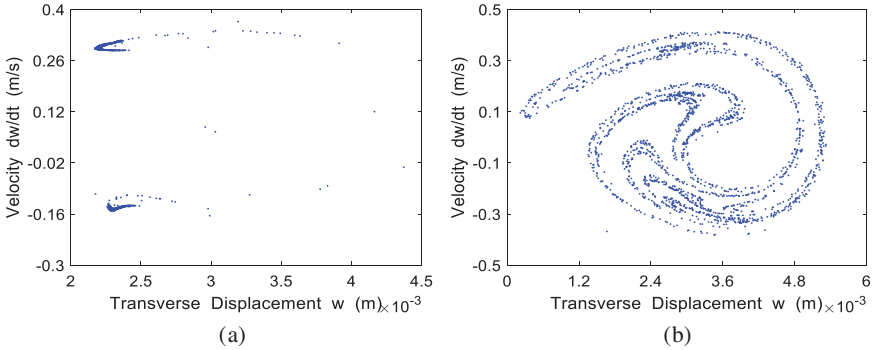

Figure 10: (Continued)

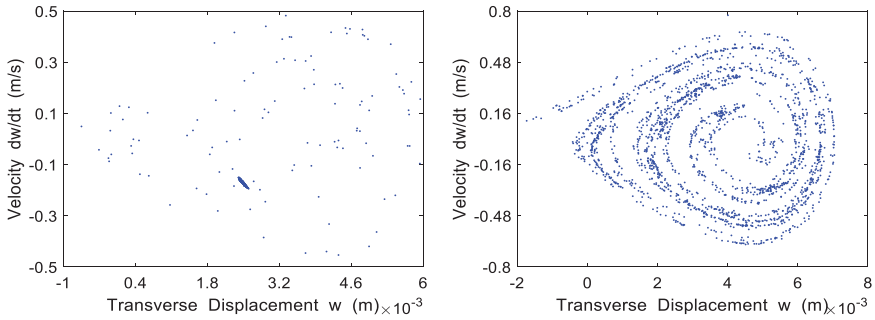

(c) (d)

Figure 10: The Poincaré map of the system at different incoming velocities

4.3 When the Magnetic Field Distribution B_{1z} = 7.5T

Selecting $x_4/x_1 = 27.73$, $\omega = 20$ rad/s, Fig. 11 is the bifurcation diagram of the relationship between the displacement of the mid-point of the plate and the incoming velocity U. As can be seen from Fig. 11, periodic vibration and chaotic motion appear alternately. Compared with Figs. 3 and 7, the multiply-periodic motion region is further reduced in Fig. 11. At this point, the discriminative region of chaos is further changed due to the enhancement of the magnetic field. At this point, the magnetic field not only plays a damping role, but also reduces the stability of the system.

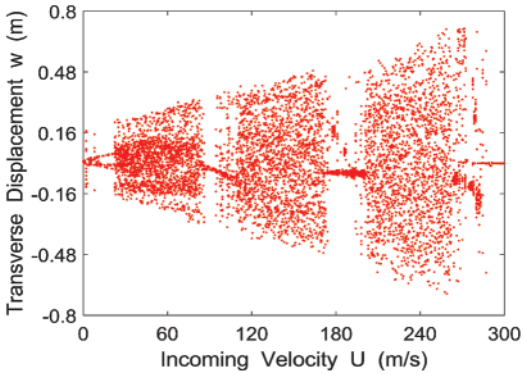

Figure 11: Bifurcation diagram of the lateral displacement of the midpoint of the rectangular conductive thin plate with respect to the incoming velocity

Take $U = 100$ m/s, $U = 150$ m/s, $U = 200$ m/s, and $U = 250$ m/s into Eq. (53), respectively. When $U = 100$ m/s, $2\sqrt{2} \times x_2^{1.5}/3\pi\sqrt{x_3}\left[\omega \times \text{csch}\left(\omega\pi/2\sqrt{x_2}\right)\right] = 0.015 < x_4/x_1 = 27.73$, satisfying the discriminant condition for the existence of chaos; when $U = 150$ m/s, $2\sqrt{2} \times x_2^{1.5}/3\pi\sqrt{x_3}\left[\omega \times \text{csch}\left(\omega\pi/2\sqrt{x_2}\right)\right] = 0.067 < x_4/x_1 = 27.73$, satisfying the discriminant condition for the existence of chaos; when $U = 200$ m/s, $2\sqrt{2} \times x_2^{1.5}/3\pi\sqrt{x_3}\left[\omega \times \text{csch}\left(\omega\pi/2\sqrt{x_2}\right)\right] = 0.139 < x_4/x_1 = 27.73$, satisfying the discriminant condition for the existence of chaos; when $U = 250$ m/s, $2\sqrt{2} \times x_2^{1.5}/3\pi\sqrt{x_3}\left[\omega \times \text{csch}\left(\omega\pi/2\sqrt{x_2}\right)\right] = 0.231 < x_4/x_1 = 27.73$, satisfying the discriminant condition for the existence of chaos. From this, the time history response, phase portrait and Poincaré map of the system are drawn. The change in magnetic field only changes the value of x_4/x_1 and does not affect the value of $2\sqrt{2} \times x_2^{1.5}/3\pi\sqrt{x_3}\left[\omega \times \text{csch}\left(\omega\pi/2\sqrt{x_2}\right)\right]$. Even if there are different magnetic field distributions, the critical surface remains the same if the incoming velocity is constant. The presence

of the magnetic field further expands the chaotic region of the system, in which the magnetic field also acts as a damping agent.

The time-history curve for the four cases of $U = 100$ m/s, $U = 150$ m/s, $U = 200$ m/s, and $U = 250$ m/s, are shown in Figs. 12a–12d. As can be seen from Fig. 12, the time history response of the system has no periodicity at all, which indicates that the motion of the system presents a chaotic nature at this time. When the magnetic field strength is 7.5T (constant magnetic field strength), the incoming velocity affects the amplitude of the system vibration as well as the stability of the motion. And compared to the two cases of magnetic field strength of 0T and 5T, the regularity of the system motion further decreases.

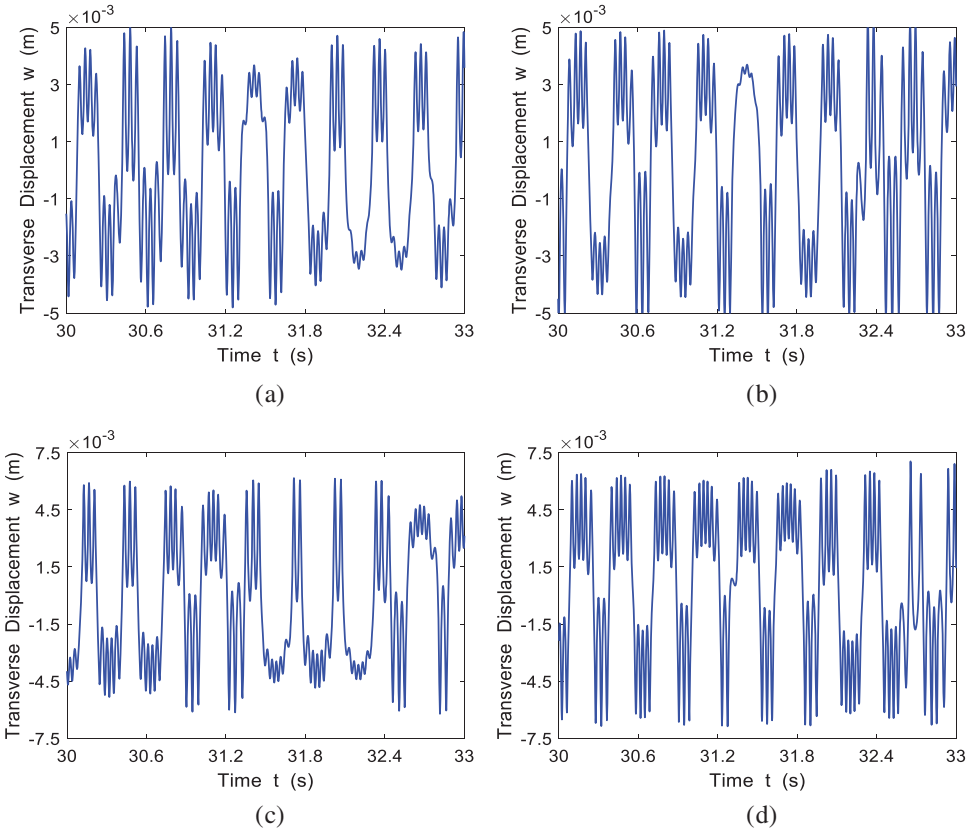

Figure 12: The time history response of the system at different incoming velocities

The phase portrait for the four cases of $U = 100$ m/s, $U = 150$ m/s, $U = 200$ m/s, and $U = 250$ m/s are shown in Figs. 13a–13d. As can be seen from Fig. 13, there are many unclosed limit cycles in the phase portrait of the system, which are restricted to a bounded region, which indicates that the motion of the system presents a chaotic nature at this time. Fig. 13c shows a further decrease in the stability compared to Fig. 9c, which is clearly a result of the chaotic region being further expanded due to the increase in magnetic field strength that drives the chaotic region.

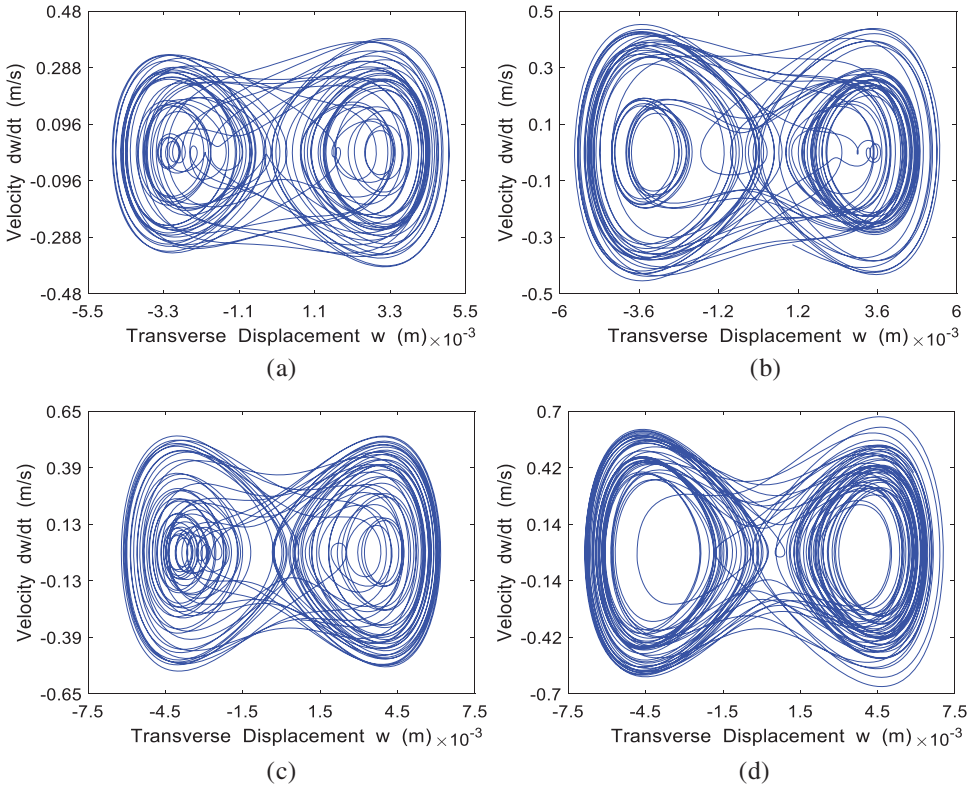

Figure 13: The phase portrait of the system at different incoming velocities

The Poincaré map for the four cases of $U = 100$ m/s, $U = 150$ m/s, $U = 200$ m/s, and $U = 250$ m/s are shown in Figs. 10a–10d. As can be seen from the Poincaré map, there is a fractal structure of dense points in the cross section, which is neither a finite set of points nor a closed curve, which indicates that the motion of the system at this time presents a chaotic state. Fig. 14 shows a more chaotic state compared to Figs. 10 and 6, which indicates that the increase in magnetic field strength makes the stability of the system motion further reduced.

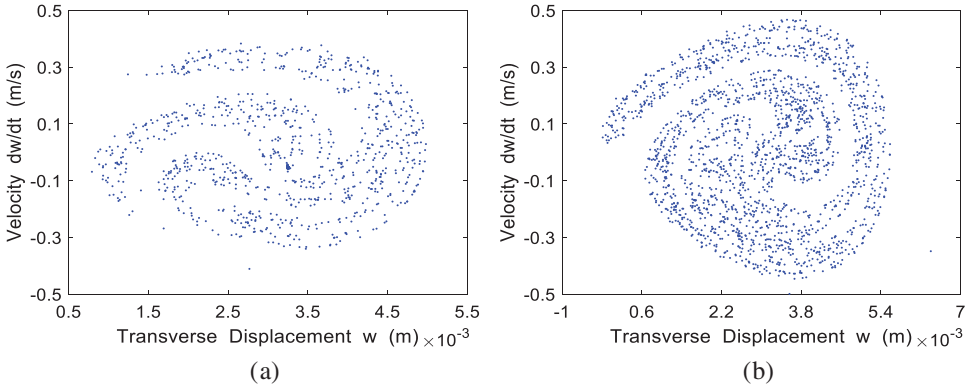

Figure 14: (Continued)

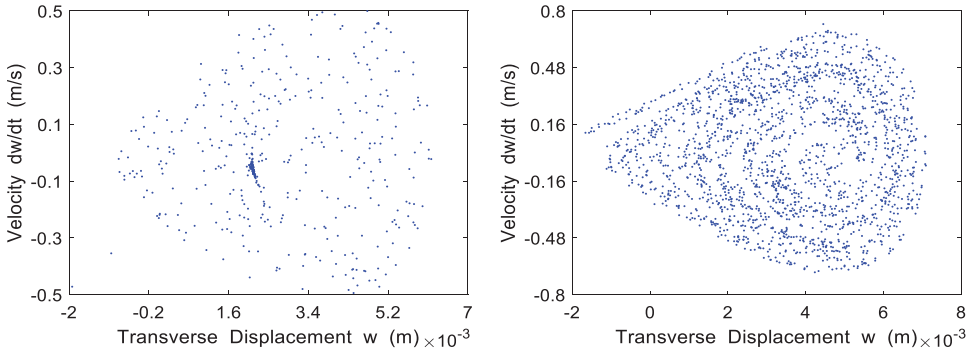

Figure 14: The Poincaré map of the system at different incoming velocities

5 Results and Discussion

In this paper, the effects of incoming velocity, magnetic field, and periodic mechanical force on the kinematic behavior of a rectangular conductive thin plate are studied. According to Kirchhoff's thin plate theory, considering the geometric nonlinearity, the nonlinear dynamic equation of the system motion is established by using the principle of virtual work. The Galerkin's method is used and the Hamiltonian system is introduced to analyze the Hamiltonian system with Melnikov functions to obtain the criterion for the existence of chaos. The bifurcation diagram, time history response, phase portrait and Poincaré map of the system under different magnetic field strengths are obtained through MATLAB simulation, and the chaotic motion of the rectangular conductive thin plate is qualitatively analyzed. Numerical results verify the possibility of chaotic behavior when the structural parameters given by the theoretical analysis satisfy certain conditions.

(1) Based on the theoretical analysis and numerical calculation results, the chaotic motion is related to the incoming velocity and the magnetic field strength. When $x_4/x_1 > 2\sqrt{2} \times x_2^{1.5}/3\pi\sqrt{x_3}\left[\omega \times \operatorname{csch}\left(\omega\pi/2\sqrt{x_2}\right)\right]$, that is, when the ratio of external excitation amplitude to damping coefficient is higher than the critical plane, the system will enter chaotic state. Therefore, the stability of the system can be judged by the ratio of external excitation amplitude to damping coefficient. For the nonlinear vibration of the rectangular thin plate, the selection of different initial values will have a greater impact on the kinematics of the system.

(2) The change of magnetic field only changes the value of x_4/x_1 and does not affect the value of the critical surface. With different magnetic field distributions, the critical surface remains the same if the incoming velocity is constant. Therefore, the presence of the magnetic field further expands the chaotic region of the system, in which the magnetic field also acts as a damping effect and reduces the stability of the system.

(3) With the constant change of the incoming velocity, the motion of the rectangular conductive thin plate will enter an unstable state, resulting in chaotic motion. The increase of the magnetic field strength B_{1z} also has a certain influence on the motion behavior of the rectangular thin plate. Therefore, the nonlinear dynamic behavior of the rectangular conductive thin plate model can be controlled by varying the incoming velocity and magnetic field strength, respectively.

Funding Statement: This research was funded by the Anhui Provincial Natural Science Foundation (Grant No. 2008085QE245), the Natural Science Research Project of Higher Education Institutions in Anhui Province (2022AH040045), the Project of Science and Technology Plan of Department of Housing and Urban-Rural Development of Anhui Province (2021-YF22).

Conflicts of Interest: The authors declare that they have no conflicts of interest to report regarding the present study.

References

1. Dowell, E. H. (1979). Aeroelasticity of plates and shells. *ZAMM-Journal of Applied Mathematics and Mechanics, 59(10),* 585–585.
2. Li, S. B., Hao, X. Y. (2012). Chaotic motion of a functionally graded materials square thin plate. *Advanced Materials Research, 1839(531),* 593–596. https://doi.org/10.4028/www.scientific.net/AMR.531.593
3. Abdulrazzaq, M. A., Muhammad, A. K., Kadhim, Z. D., Faleh, N. M. (2020). Vibration analysis of nonlocal strain gradient porous FG composite plates coupled by visco-elastic foundation based on DQM. *Coupled Systems Mechanics, 9(3),* 201–217.
4. Zhang, W., Chen, J. E., Gao, D. X., Chen, L. H. (2014). Nonlinear dynamic responses of a truss core sandwich plate. *Composite Structures, 108,* 367–386. https://doi.org/10.1016/j.compstruct.2013.09.033
5. Dugundjim, J., Dowell, E. H., Perkin, B. (1963). Subsonic flutter of panels on continuous elastic foundations. *AIAA Journal, 1(5),* 1146–1154. https://doi.org/10.2514/3.1738
6. Tang, M., Tang, J. F., Zhou, D. S., Yu, D. R. (2021). Nonlinearity of initiating and extinguishing boundaries of DBDs with airflows. *Plasma Science and Technology, 23(6)*. https://doi.org/10.1088/2058-6272/abea05
7. Zhao, K., He, D. W., Fu, S. H., Bai, Z. Y., Miao, Q. et al. (2022). Interfacial coupling and modulation of van der waals heterostructures for nanodevices. *Nanomaterials, 12(19),* 3418–3418. https://doi.org/10.3390/nano12193418
8. Kumar, A., Khurana, A., Sharma, A. K., Joglekar, M. M. (2022). Dynamics of pneumatically coupled visco-hyperelastic dielectric elastomer actuators: Theoretical modeling and experimental investigation. *European Journal of Mechanics-A/Solids, 95*. https://doi.org/10.1016/j.euromechsol.2022.104636
9. Tang, D. M., Henry, J. K., Dowell, E. H. (1999). Limit cycle oscillations of delta wing models in low subsonic flow. *AIAA Journal, 37(11),* 1355–1362. https://doi.org/10.2514/2.627
10. Qiao, Y., Yao, G. (2022). Stability and nonlinear vibration of an axially moving plate interacting with magnetic field and subsonic airflow in a narrow gap. *Nonlinear Dynamics, 110(4),* 3187–3208. https://doi.org/10.1007/s11071-022-07805-9
11. Zhang, D. C., Li, P., Zhu, Y. Z., Yang, Y. R. (2022). Aeroelastic instability of an inverted cantilevered plate with cracks in axial subsonic airflow. *Applied Mathematical Modelling, 107,* 782–801. https://doi.org/10.1016/j.apm.2022.03.019
12. Ge, G., Zhu, W. Z. (2011). An improved way of detecting the threshold value of chaotic motion on a parametrical excited rectangular thin plate. *Applied Mechanics and Materials, 1326(66),* 833–837. https://doi.org/10.4028/www.scientific.net/AMM.66-68.833
13. Hu, Y. D., Li, J. (2008). The magneto-elastic combination resonances analysis of current-conducting thin plate in magnetic field. *Journal of Sound and Vibration, 29(8),* 1053–1066.
14. Hu, Y. D., Li, J. (2008). Nonlinear magneto-elastic vibrating equations and response analysis of a current-conducting thin plate. *International Journal of Structural Stability and Dynamics, 8(4),* 597–613. https://doi.org/10.1142/S0219455408002855
15. Li, J., Hu, Y. D., Wang, Y. N. (2017). The magneto-elastic internal resonances of rectangular conductive thin plate with different size ratios. *Journal of Mechanics, 34(5),* 711–723. https://doi.org/10.1017/jmech.2017.30

16. Pao, Y. H., Yeh, C. S. (1973). A linear theory for soft ferromagnetic elastic solids. *International Journal of Engineering Science, 11(4),* 415–436. https://doi.org/10.1016/0020-7225(73)90059-1
17. Sh, E. L., Kattimani, S., Vinyas, M. (2022). Nonlinear free vibration and transient responses of porous functionally graded magneto-electro-elastic plates. *Archives of Civil and Mechanical Engineering, 22(1)*. https://doi.org/10.1007/s43452-021-00357-6
18. Chen, J. E., Liu, Y. Q., Liu, W., Su, X. Y. (2013). Themal buckling analysis of truss core sandwich plates. *Applied Mathematics and Mechanics, 34(10),* 1177–1186. https://doi.org/10.1007/s10483-013-1737-9
19. Chen, J. E., Zhang, W., Yao, M. H., Liu, J. (2018). Vibration reduction in truss core sandwich plate with internal nonlinear energy sink. *Composite Structures, 193,* 180–188. https://doi.org/10.1016/j.compstruct.2018.03.048
20. Agarwal, S., Dash, B., Saini, P., Sharma, N., Mahapatra, T. R. et al. (2020). Vibroacoustic analysis of un-baffled layered composite plate under thermal environment. *Materials Today: Proceedings, 24(2),* 1020–1028.
21. Liu, Y. F., Qin, Z. Y., Chu, F. L. (2022). Investigation of magneto-electro-thermo-mechanical loads on nonlinear forced vibrations of composite cylindrical shells. *Communications in Nonlinear Science and Numerical Simulation, 107*. https://doi.org/10.1016/j.cnsns.2021.106146
22. Liu, Y. F., Qin, Z. Y., Chu, F. L. (2021). Nonlinear forced vibrations of functionally graded piezoelectric cylindrical shells under electric-thermo-mechanical loads. *International Journal of Mechanical Sciences, 201,* 106474. https://doi.org/10.1016/j.ijmecsci.2021.106474
23. Malikan, M., Eremeyev, V. A. (2022). The effect of shear deformations' rotary inertia on the vibrating response of multi-physic composite beam-like actuators. *Composite Structures, 297,* 115951. https://doi.org/10.1016/j.compstruct.2022.115951
24. Malikan, M., Eremeyev, V. A. (2022). Flexomagneticity in buckled shear deformablehard-magnetic soft structures. *Continuum Mechanics and Thermodynamics, 34,* 1–16. https://doi.org/10.1007/s00161-021-01034-y
25. Gladkov, S. O. (2021). Theory of electromagnetic radiation by inertially moving conductive bodies. *Journal of Communications Technology and Electronics, 66(6),* 690–693. https://doi.org/10.1134/S1064226921060115
26. Zhang, J., Shen, X., Wang, Y., Ji, C., Zhou, Y. et al. (2020). Design of two-dimensional multiferroics with direct polarization-magnetization coupling. *Physical Review Letters, 125(1),* 017601. https://doi.org/10.1103/PhysRevLett.125.017601
27. Moon, F. C., Holmes, P. J. (1979). A magnetoelastic strange attractor. *Journal of Sound and Vibration, 65(2),* 275–296. https://doi.org/10.1016/0022-460X(79)90520-0
28. Wen, H. H., Duan, Y. H., Pan, L. X. (1997). An analytical study for controlling unstable, periodic motion in magneto-elastic chaos. *Physics Letter A, 234(3),* 198–204. https://doi.org/10.1016/S0375-9601(97)00501-X
29. Lu, Q. S., To, C. W. S., Huang, K. L. (1995). Dynamic stability and bifurcation of an alternating load and magnetic field excited magnetoelastic beam. *Journal of Sound and Vibration, 181(5),* 873–891. https://doi.org/10.1006/jsvi.1995.0175
30. Ershkov, S. V., Leshchenko, D., Giniyatullin, A. R. (2021). A new solving procedure for the kelvin–Kirchhoff equations in case of a falling rotating torus. *International Journal of Bifurcation and Chaos, 31(1)*. https://doi.org/10.1142/S0218127421500103
31. Ogawa, S., Hamauzu, S., Kikuma, T. (2000). A notion of strain and stress tensor for finite deformation of elastic-plastic continua. *Journal of the Society of Materials Science, 49(6),* 80–87. https://doi.org/10.2472/jsms.49.6Appendix_80
32. Sokhal, S., Verma, S. R. (2021). A Fourier wavelet series solution of partial differential equation through the separation of variables method. *Applied Mathematics and Computation, 388*. https://doi.org/10.1016/j.amc.2020.125480

33. Li, P., Yang, Y. R., Zhang, M. L. (2011). Melnikov's method for chaos of a two-dimensional thin panel in subsonic flow with external excitation. *Mechanics Research Communications, 38(7),* 524–528. https://doi.org/10.1016/j.mechrescom.2011.07.008
34. Ge, H. X., Zhu, T. (1998). A new meshless local petrov-galerkin (MLPG) approach in computational mechanics. *Computational Mechanics, 22,* 117–127. https://doi.org/10.1007/s004660050346
35. Chen, F. F., Qian, D. B. (2022). An extension of the Poincaré-Birkhoff theorem for Hamiltonian systems coupling resonant linear components with twisting components. *Journal of Differential Equations, 321,* 415–448. https://doi.org/10.1016/j.jde.2022.03.016
36. Chen, L. Q. (1991). The necessary condition for the appearance of chaos in two classes of forced vibration system with both square and cubic nonlinear terms. *Acta Mechanica Solida Sinica, 4(4),* 381–386.
37. Wiggins, S. (1988). *Global bifurcations and chaos*. New York: Springer Verlag.
38. Wiggins, S. (1990). *Introduction to applied nonlinear dynamical systems and chaos*. New York: Springer Verlag.
39. Feng, J. H., Li, Y. (2021). The weak smale horseshoe and mean hyperbolicity. *Journal of Differential Equations, 299,* 154–195. https://doi.org/10.1016/j.jde.2021.07.020